Enhanced High-Temperature Thermoelectric Performance by Strain Engineering in BiOCl

Cheng-Wei Wu,[1] Xue Ren,[1] Guofeng Xie,[1] Wu-Xing Zhou[1],[*] Gang Zhang,[2],[†] and Ke-Qiu Chen[3],[‡]

[1]*School of Materials Science and Engineering & Hunan Provincial Key Laboratory of Advanced Materials for New Energy Storage and Conversion, Hunan University of Science and Technology, Xiangtan 411201, China*
[2]*Institute of High Performance Computing A*STAR, Singapore 138632, Singapore*
[3]*Department of Applied Physics, School of Physics and Electronics, Hunan University, Changsha 410082, China*

Semiconductor BiOCl has a layered structure with ultralow lattice thermal conductivity [Q.D. Gibson *et al.*, Science 373, 1017–1022 (2021)] and has potential applications in the field of thermoelectric materials. In the present study, the thermoelectric properties of BiOCl crystals are accurately predicted using the first-principles calculation combined with Boltzmann transport theory. The dimensionless figure of merit (*ZT*) of *p*-type BiOCl is found to be 0.2 at room temperature, reaching 1.1 at 800 K. In addition, applying in-plane biaxial tensile strain ϵ_{xy} can lead to a further increase in the value of *ZT* to 1.9 at 800 K. This means that *p* BiOCl is an excellent high-temperature thermoelectric material. And this is due to the fact that biaxial strain drastically reduces the lattice thermal conductivity and the shift of the valence band toward the Fermi level can optimize the carrier concentration. Thus, the present work paves a way for the design of adjustable high-temperature thermoelectric materials.

I. INTRODUCTION

Thermoelectric (TE) materials can convert thermal energy directly into electric power without noise and pollution [1–4]. This property can be used to replace compression refrigeration, generate electricity, and so on, which provides effective ways to solve the global energy crisis [5]. At present, the performance of thermoelectric materials is usually evaluated by the dimensionless figure of merit, $ZT = S^2 \sigma T / (\kappa_e + \kappa_p)$, where S is the Seebeck coefficient, σ is the electrical conductivity, κ_e is the electronic thermal conductivity, κ_p is the lattice thermal conductivity, and T is the absolute temperature [6,7]. In this respect, the higher *ZT* value means the better efficiency η of thermoelectric conversion [8–10].

However, due to the Wiedemann-Franz law, [11] the improvement of *ZT* is a complex problem caused by the coupling between electron transport coefficients. Besides, Hick *et al.* have established that quantum confinement in low-dimensional structures on electrons and phonons can greatly improve the value of *ZT* [12]. Slack *et al.* put forward the concepts of "phonon glass, electronic crystal," and so on [9] with the aim of increasing the power factor $PF = S^2 \sigma$ and reducing thermal conductivity

[13,14]. Based on this, many advanced methods were afterwards proposed to improve the thermoelectric properties of materials. Among them, the application of heterointerfaces [15–18] and superlattices [19,20], lattice-strain engineering [21–25], as well as the insertion of dopants [26,27], amorphous phases [28], vacancy defects [29,30], and others [31–38]. In particular, lattice-strain engineering can reduce the thermal conductivity and adjust the electronic structure. This results in band degeneracy and band convergence and thereby significantly improves the thermoelectric properties of the materials.

For instance, Wu *et al.* [22] reported that lattice strain enabled to significantly decrease the lattice thermal conductivity and valence-band convergence and successfully increase the TE properties in the $Na_{0.03}Eu_{0.03}Sn_{0.02}Pb_{0.92}Te$ alloy without reducing the carrier mobility in the latter. Lin *et al.* [23] have found via the first-principles calculation that tensile strain exerts a positive influence on the thermoelectric properties of LaP and LaAs. For example, 2% tensile strain at 1200 K allowed one to achieve $ZT > 2$, being 90% higher than the original LaP. Guo [24] studied the effect of biaxial strain on the TE properties of monolayer $PtSe_2$ by applying the first-principles approaches. Their results revealed that using biaxial tensile strain of 4.02% could induce the band convergence and increase the Seebeck coefficient at reducing the room-temperature lattice thermal conductivity by 60%. Performing the first-principles calculations on the

---

[*]wuxingzhou@hnu.edu.cn
[†]zhangg@ihpc.a-star.edu.sg
[‡]keqiuchen@hnu.edu.cn

monolayer InSe, Wang *et al.* [25] found that tensile strain enhanced the anharmonic phonon scattering, thus increasing the phonon scattering rate and reducing the phonon group velocity and heat capacity of the material under consideration. Specifically, applying 6% strain was shown to decrease the lattice thermal conductivity from 25.9 to 13.1 Wm^{-1} K^{-1}.

In recent years, semiconductor BiOCl materials with layered structure have attracted considerable attention due to high chemical stability, nontoxicity, and excellent optical and electrical properties, finding application in the fields of ultraviolet light detection [39], nitrogen fixation [40], and so on [41–43]. However, the researches on the thermoelectric characteristics of BiOCl are still scarce. Recently, Gibson *et al.* [20] reported the ultralow lattice thermal conductivity, endowing BiOCl with outstanding thermoelectric potential. Therefore, the present work aims to systematically study the thermoelectric properties of BiOCl under in-plane axial strain.

II. COMPUTATION METHOD

The Vienna *ab initio* simulation package (VASP) program is used for the first-principles calculation based on density-functional theory (DFT) [44]. The exchange-correlation function adopts the generalized gradient approximation (GGA) in the form of Perdew-Burke-Ernzerhof (PBE) [45]. Among them, the total energy convergence criterion of 10^{-6} eV, the force convergence criterion of 10^{-4} eVÅ^{-1}, and the kinetic energy cutoff of 500 eV are used to optimize crystals. For thermal transport, $4 \times 4 \times 2$ supercells and Γ-center k mesh of $1 \times 1 \times 1$ are used to obtain harmonic atomic force constants matrix (second FC) and anharmonic atomic force constants matrix (third FC). In BiOCl crystals, each primitive cell contains six atoms. When calculating the second FCs and the third FCs, we set the maximum distance among the third nearest-neighbor atom to distance cutoff. Considering the symmetry of the crystal structure, the second FCs and the third FCs can be obtained by performing 6 and 180 displacement calculations, respectively [46]. According to the second FC, the phonon spectrum is calculated by Phonopy code [21,47]. Moreover, combined with the second FC and third FC, the lattice thermal conductivity can be obtained by solving the phonon Boltzmann transport equation via the ShengBTE package [46], and $25 \times 25 \times 15$ q mesh to ensure the convergence. In addition, we also use the born effective charge and dielectric tensor, which are obtained by density-functional perturbation theory (DFPT), to consider longitudinal and transverse optical phonon (LO-TO) splitting for thermal transport [48].

In this study, the influence of spin-orbit coupling (SOC) is included in the calculation of electronic structure, and the TE transport coefficients are calculated by solving the

Boltzmann transport equations via the BoltzTraP2 package [23,49–51]. Dense k mesh of $30 \times 30 \times 20$ is used to obtain the charge density. Moreover, the carrier relaxation time τ_e is calculated by Matthiessen's rule:

$$\frac{1}{\tau_e} = \frac{1}{\tau_{ac}} + \frac{1}{\tau_{imp}} + \frac{1}{\tau_{pol}}, \quad (1)$$

where τ_{ac}, τ_{imp}, and τ_{pol}, respectively, represent the relaxation time of acoustic phonon scattering, impurity scattering, and polarized phonon scattering. Among them, according to deformation potential (DP) theory, in the three-dimensional system, the relaxation time τ_{ac} can be expressed as [52,53]

$$\tau_{ac} = \frac{2\sqrt{2\pi}C_{3D}\hbar^4}{3(k_B T)^{3/2}(m^*)^{3/2}E_{DP}^2} \quad (2)$$

where $\hbar$, k_B, T are the reduced Planck constant, the Boltzmann constant and absolute temperature, respectively. The C_{3D} is the elastic modulus the E_{DP} is the DP constant, which can be calculate as [21]

$$E_{DP} = \frac{\partial E_{edge}}{\partial(\partial l/l_0)}, \quad (3)$$

where E_{edge}, $\partial l/l_0$ are the conduction-band minimum (CBM) or the valence-band maximum (VBM) and the elastic strain, respectively. The m^* is the carrier effective mass, which can be obtained as [21]

$$m^* = \frac{1}{\hbar^2}\frac{\partial^2 E}{\partial k^2}, \quad (4)$$

where E, k are the electron energy and the wave vector, respectively. In addition, both DP constant E_{DP} and carrier effective mass m^* need to calculate the band structure. The shifts of VBM, CBM as a function of strain can be used to calculate DP constant [see Fig. S1(a) and S1(b) within the Supplemental Material [54]] and the theoretical parameters of the deformation potential are all shown in Table S1 within the Supplemental Material [55]. The τ_{imp} and τ_{pol} are calculated by Casu's PYTHON code [56], and the formulas for τ_{imp} can be expressed as

$$\tau_{imp} = \frac{\sqrt{2m^*}(4\pi\epsilon_0\epsilon_s)^2}{\pi n_I Z_I^2 e^4 E^{-3/2}}\left[\log\left(1 + \frac{1}{x}\right) - \frac{1}{1+x}\right]^{-1} \quad (5)$$

$$x = \frac{\hbar^2 q_0^2}{8m^* E} \quad (6)$$

$$q_0 = \sqrt{\frac{e^2 n_I}{\epsilon_0 \epsilon k_B T}} \quad (7)$$

where ϵ_0, ϵ_s are the the vacuum permittivity and static dielectric constants, respectively, n_I is the ionized impurity concentration, Z_I is the the impurity charge and q_0 is

the Debye screening wavevector. The formulas for τ_{pol} can be expressed as

$$\tau_{\mathrm{pol}} = \left[\sum_i \frac{C(T,E,e_i^{\mathrm{LO}}) - A(T,E,e_i^{\mathrm{LO}}) - B(T,E,e_i^{\mathrm{LO}})}{Z(T,E,e_i^{\mathrm{LO}})E^{3/2}} \right]^{-1},$$

(8)

$$A = \underbrace{(n(\omega_{\mathrm{LO}})+1)}_{A_0} \frac{f(x)}{f(E)} \left[(E+x)\sinh^{-1}(\sqrt{w}) - (Ex)^{1/2} \right],$$

(9)

$$B = \underbrace{\theta(y)n(\omega_{\mathrm{LO}})}_{B_0} \frac{f(y)}{f(E)} \left[(E+y)\cosh^{-1}(\sqrt{w}) - (Ey)^{1/2} \right],$$

(10)

$$C = 2E \left[A_0 \frac{f(x)}{f(E)}\sinh^{-1}(\sqrt{w}) + B_0 \frac{f(y)}{f(E)}\cosh^{-1}(\sqrt{w}) \right],$$

(11)

$$Z = \frac{2}{W_0\sqrt{\hbar\omega_{\mathrm{LO}}}}; \ W_0 = \frac{e^2}{4\pi\hbar}\sqrt{\frac{2m^*\omega_{\mathrm{LO}}}{\hbar}} \left(\frac{1}{\epsilon_\infty} - \frac{1}{\epsilon_s} \right),$$

(12)

where $e_i^{\mathrm{LO}} = \hbar\omega_{\mathrm{LO}}$ is the energy of longitudinal-optical phonons, ω_{LO} is the longitudinal optical angular frequency, f is the Fermi-Dirac function, $n(\omega_{\mathrm{LO}})$ is the phonon occupation number that follows the Planck distribution and ϵ_∞ is the the high-frequency dielectric constants. x, y, and w are defined as $E + e_i^{\mathrm{LO}}$, $E - e_i^{\mathrm{LO}}$, and E/e_i^{LO}, respectively. In addition, the required parameters are presented within the Supplemental Material (Table S2 [57]).

III. RESULTS AND DISCUSSION

Figures 1(a) and 1(b) display the side and top views of the optimized structure of BiOCl, respectively. The unit cell of BiOCl contains a pair of Bi atoms, a pair of Cl atoms, and a pair of O atoms, and belongs to a simple tetragonal lattice system. The bulk BiOCl possesses a layered structure wherein the intralayer direction (a and b axes) is collectively referred to as in-plane direction (in plane, $\parallel$), and the interlayer direction direction (c axis) is out-of-plane direction (out plane, $\perp$). The optimized lattice constants are $a = b = 3.90$ Å and $c = 7.42$ Å, which are in good agreement with the experimental values $a = b = 3.89$ Å and $c = 7.37$ Å [41].

Figure 1(c) depicts the phonon spectrum of BiOCl, calculated by finite displacement method. There is no imaginary frequency in the first Brillouin zone (BZ), which provides evidence of lattice stability. Moreover, the phonon modes along the $\Gamma - Z$ direction are flatter than those along the $\Gamma - X$ direction, indicating that the group velocity of the phonon modes and the lattice thermal conductivity along the out plane are lower than those along the in plane. Figure 1(d) shows the energy band structure of BiOCl, allowing one to classify it as the indirect bandgap semiconductor. The CBM is located at the Z point of the BZ, and the VBM is near the R point. Considering that PBE usually underestimates the band gap, the HSE function is used to correct it. In Figs. 1(c) and 1(d), it is not difficult to find that the band gap has increased from 2.3 eV (PBE+SOC) to 3.49 eV (PBE+SOC+HSE), which is in good agreement with the experimental data (3.57 eV).

In order to understand the TE performance of BiOCl, the electrical and thermal transport properties of BiOCl are
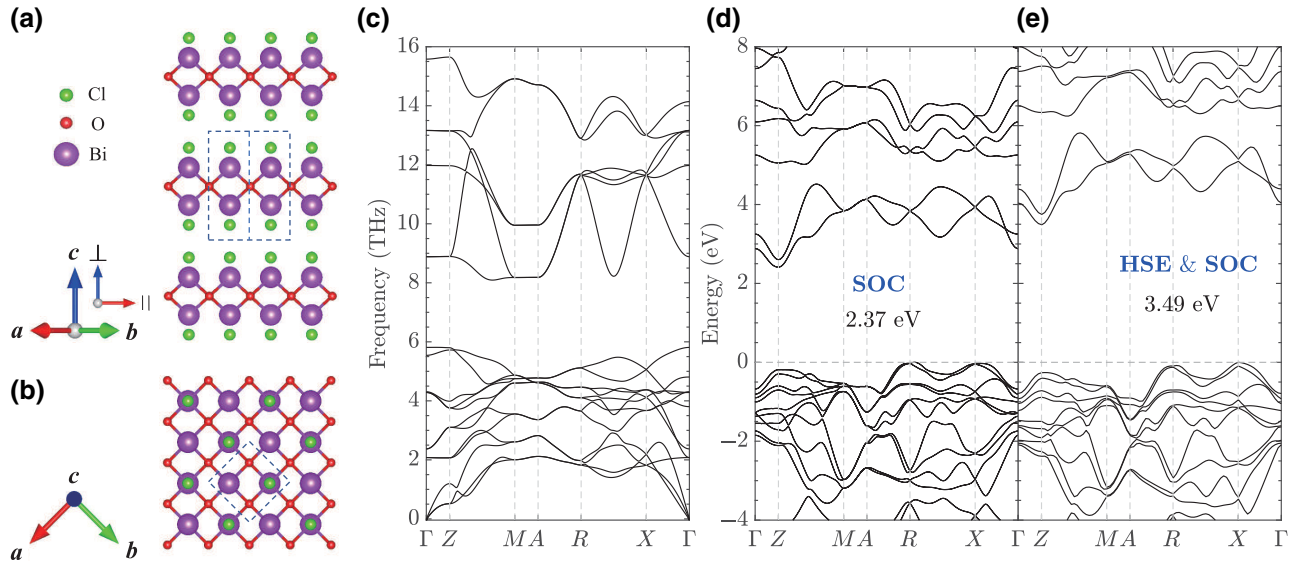

FIG. 1. (a) The side view and (b) the top view of the optimized structure of BiOCl. (c) The phonon spectrum of BiOCl. (d) The electronic energy bands of BiOCl (PBE+SOC). (e) The electronic energy bands of BiOCl (PBE+SOC+HSE).
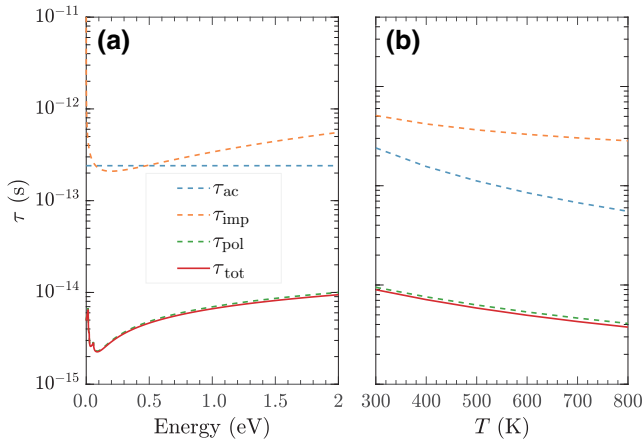
FIG. 2. (a) The relaxation time τ of p-type BiOCl as a function of electron energy E ($T = 300$ K). (b) The relaxation time τ of p-type BiOCl as a function of temperature T ($E = 1.8$ eV above the conduction edge).

systematically calculated. We find that the p-type BiOCl is more suitable for thermoelectric materials compared with the n-type BiOCl, and the peak values of ZT are equal to 0.05 and 0.2 along the in-plane and the out-plane orientation, respectively, at room temperature. More details can be found in the Supplemental Material [58]. Therefore, in this work, we mainly focus on the thermoelectric performance of p-type BiOCl. Considering that BiOCl is a polar material, ionized impurity scattering and polar optical phonon scattering are not negligible [56,59]. Therefore, in order to accurately describe the carrier scattering behavior of BiOCl, we calculate the acoustic phonon scattering, impurity scattering, and polarized phonon scattering. It is not difficult to find that the carrier scattering in p-type BiOCl is dominated by LO-polarized phonon scattering. In Fig. 2(a), τ_{pol} is an order of magnitude lower than τ_{ac} and τ_{imp} (doping concentration set as 10^{21} cm^{-3}), and these scattering behaviors become stronger with the increase of temperature as shown in Fig. 2(b).

Figures 3(a)–3(c) and 3(d)–3(f) display the κ_e, PF, and ZT parameters of p-type BiOCl along in plane and out plane, respectively, as functions of carrier concentration n at different temperatures. We can see that BiOCl is a potential high-temperature thermoelectric candidate material. Moreover, the thermoelectric performance of BiOCl within the same temperature range monotonously increased. From 300 to 800 K, the ZT peaks (ZT_{max}) of p-type BiOCl along in plane increased from 0.05 to 0.3, and that along out plane increased from 0.2 to 1.1. It is not difficult to find that the ZT peaks of out plane is one order of magnitude almost higher than the ZT peaks of in plane, so the p-type BiOCl along out plane is more suitable for TE transport compared with the p-type BiOCl along in plane. Observing the behavior of κ_e and PF parameters at various carrier concentrations n, a significant increase
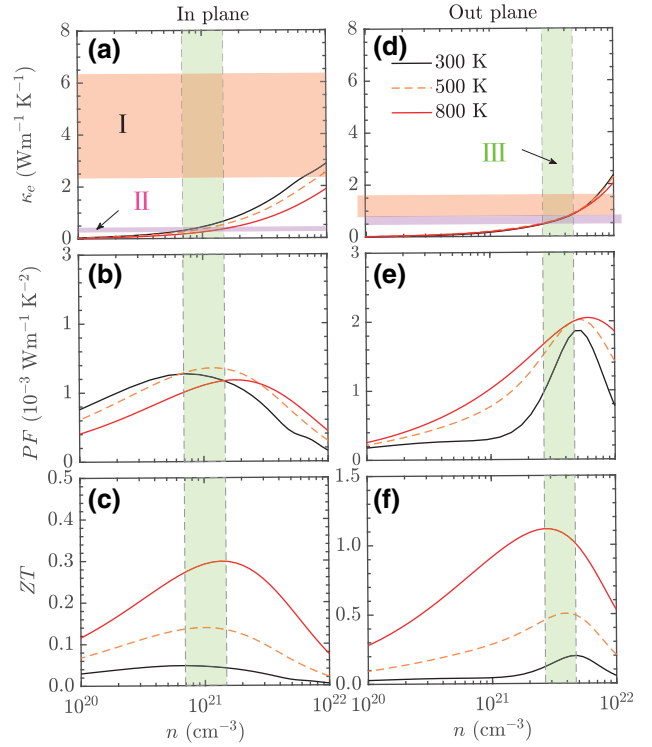

FIG. 3. The relationship between the thermoelectric transport coefficient and the carrier concentration at 300, 500, and 800 K, respectively. (a) Electron thermal conductivity, (b) power factor, and (c) ZT of p-type BiOCl along in plane. (d) Electron thermal conductivity, (e) power factor, and (f) ZT of p-type BiOCl along out plane. In this figure, the shaded areas I (yellowish-brown, longitudinal), II (purple, longitudinal), and III (green, horizontal), respectively, represent the κ_p variation, the κ_e range, and the n_{opt} range from 300 to 800 K.

in thermoelectric performance of p-type BiOCl is due to the two aspects. The first is the change of PF has almost no positive contribution to ZT as the increase of temperature, but also there is no significant reduction. The second is associated with a reduction of the total thermal conductivity. As shown in Figs. 3(a) and 3(d), regions I and II, respectively, represent the κ_p variation and the κ_e range from 300 to 800 K. It is not difficult to see that the decrease in total thermal conductivity of BiOCl is mainly provided by κ_p [Figs. 3(a) and 3(d)]. This is due to the fact that, in the temperature range of 300 to 800 K, phonons' transport is dominated by the Umklapp process, which conditioned the relationship of $\kappa_p \sim T^{-1}$ [60,61]. In turn, the decrease of κ_e is weaken. The fundamental reason is that the value n corresponding to ZT_{max}—the so-called optimal carrier concentration (n_{opt})—varied in a small range for p-type BiOCl with the increase of temperature. The width of region III, represented the n_{opt} variation from 300 to 800 K, vividly illustrates this point, as shown in Figs. 3(a) and 3(d). Since low carrier concentration means a decrease in κ_e, optimizing n_{opt} is an efficient way to improve thermoelectric
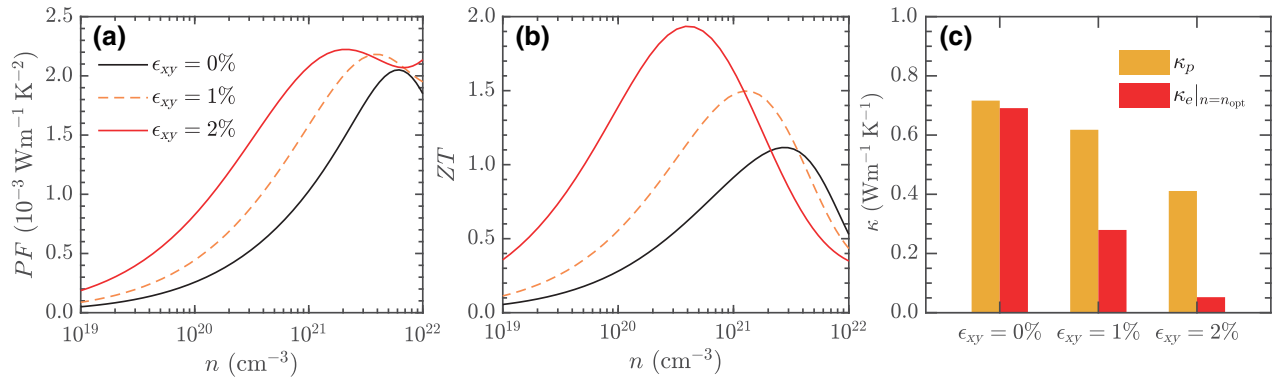
FIG. 4. The relationships between the thermoelectric transport coefficient and the carrier concentration at 800 K under biaxial strain ϵ_{xy} of 0%, 1%, and 2%. (a) PF, (b) ZT, (c) κ_p, and κ_e at n_{opt} of p-type BiOCl along out plane.

performance. Moreover, the value of n_{opt} in p-type BiOCl is found to be as high as $10^{21} \sim 10^{22}$ cm^{-3}, which would be hard to achieve experimentally. In addition, the underestimated band gap may cause n_{opt} to be underestimated. According to Jeffrey *et al.* [62], an ideal n_{opt} of the thermoelectric material should be $10^{19} \sim 10^{21}$ cm^{-3}. Therefore, optimization of n_{opt} is a reliable mean to enhance thermoelectric performance.

For this purpose, strain engineering can be theoretically applied. In that regard, a small in-plane biaxial tensile strain ($\epsilon_{xy} \leq 2\%$) is further simulated in the in plane. As seen from the plots in Fig. 4(b), the in-plane biaxial tensile strain exerted a positive effect on the ZT values of p-type BiOCl. At 800 K, the values of ZT_{max} of p-type BiOCl exposed to strain of 0%, 1%, and 2%, are equal to 1.1, 1.5, and 1.9, respectively. In turn, the peak value of PF remains almost unchanged in Fig. 4(a), while κ_p decreased monotonously with the increase of ϵ_{xy} in Fig. 4(c). Moreover, according to Fig. 3(c), the reduction of κ_p usually optimizes n_{opt} to reducing κ_e and obtaining a larger Seebeck coefficient [62]. Therefore, the improvement of ZT of p-type BiOCl could be finally attributed to the decrease of κ_p. This means that ϵ_{xy} can improve the thermoelectric performance of BiOCl without affecting the electronic transport in the material. Moreover, the electron transport coefficient of p-type BiOCl moved towards the lower carrier concentrations. It is noteworthy that the value of n_{opt} of p-type BiOCl is reduced by an order of magnitude, from approximately 10^{21} to approximately 10^{20} cm^{-3}. This might be caused by the effect of in-plane strain on the electronic structure and phonon thermal conductivity. However, it is worth noting that BiSI is currently difficult to obtain high carrier concentration through defect doping, because bismuth chalcohalides has a large ionization potential [63]. Therefore, it is still a challenge to obtain high carrier concentration by doping in bismuth sulfide materials.

The impact of ϵ_{xy} on the electronic structure of BiOCl is assessed by calculating the energy band structures (see

Fig. S6 within the Supplemental Material [64]). The difference in the responses from the valence-band structure and conduction-band structure to ϵ_{xy} is obvious, the sensitivity of the valence band structure, while the conduction-band structure remains almost unchanged. Therefore, under the influence of ϵ_{xy}, the change of valence band is one of the reasons for the significant decrease of n_{opt} of p-type BiOCl. In particular, with the increase of ϵ_{xy}, the electron energy of the first valence band, located at Z point, increased gradually, approaching the Fermi level. At $\epsilon_{xy} = 2\%$, the VBM changed from around R point to Z point, which results in the transition from the indirect band gap to the direct one. Therefore, due to the increase of ϵ_{xy}, the reduction of the band gap is the direct reasons for the decrease of n_{opt}.

For phonon thermal conductivity, the introduction of ϵ_{xy} can reduce the lattice thermal conductivity. As seen in Fig. 5(a), both the in-plane ($\kappa_{p\parallel}$) and out-of-plane ($\kappa_{p\perp}$) lattice thermal conductivities significantly decreased with the increase of strain in the temperature range from 300 to 800 K. Once the value of ϵ_{xy} achieved 2%, the in-plane and out-of-plane lattice thermal conductivities are almost reduced by 50%, which is beneficial to the improvement of thermoelectric performance. This is predictable because the tensile strain weakens the bonding and enhances the anharmonic [18,65]. Moreover, the significant regulation of phonon thermal conductivity by strain engineering has also been found in other material systems [22–25]. Among them, Lin *et al.* found that 2% tensile strain can reduce the lattice thermal conductivity of LaP by 50%, while 2% compressive strain can increase the thermal conductivity of LaP by 125% [23]. In order to elucidate the circumstances of the decrease of κ_p and the effects of phonons with different frequencies, the normalized cumulative thermal conductivity is analyzed. In particular, it was found that 98% of the out-of-plane thermal conductivity and 91% of the in-plane lattice thermal conductivity were mainly derived from the low-frequency phonons ($\omega < 6$ THz) [see Figs. S7(d) and S7(e) within the Supplemental Material [66]]. Using the empirical formula $\kappa_p =$
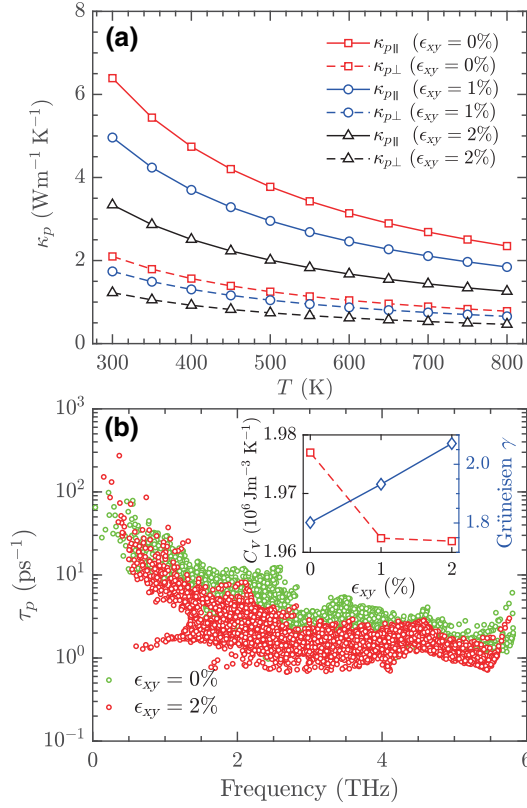
FIG. 5.   (a) In-plane lattice thermal conductivity ($\kappa_{p\parallel}$) and out-of-plane lattice thermal conductivity ($\kappa_{p\perp}$) as functions of temperature under biaxial tensile strain; (b) phonon relaxation time as a function of frequency at different biaxial tensile strains.
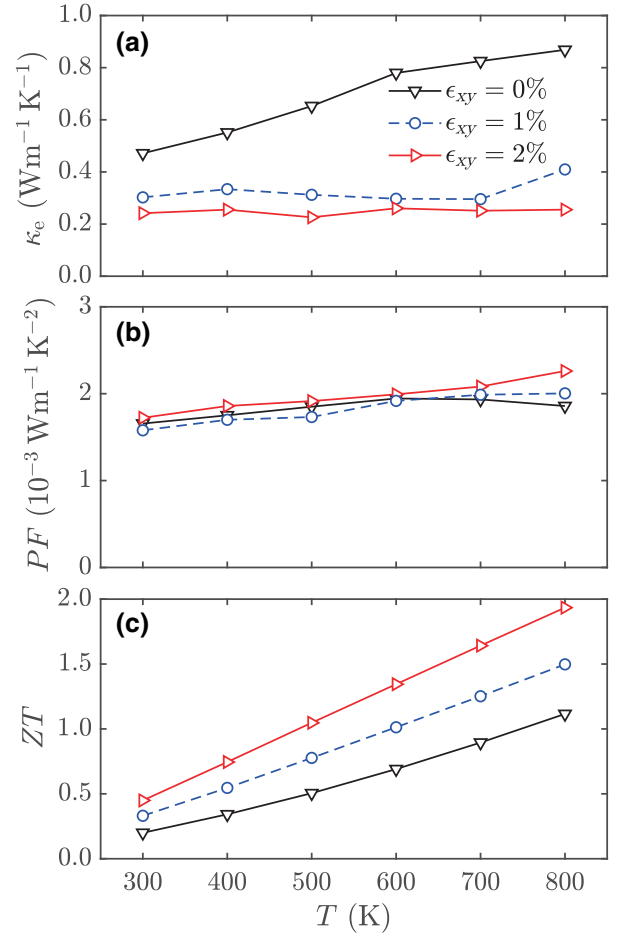

FIG. 6.   The temperature dependences at a specific strain and the optimal carrier concentration: (a) electron thermal conductivity, (b) power factor, and *ZT* of *p*-type BiOCl *p*-type BiOCl.

$1/3C_v V_g^2 \tau_p$, where C_v, V_g, and τ_p are the heat capacity, group velocity, and phonon relaxation time, respectively, the parameters C_v, V_g, and τ_p are compared afterwards under different strains at 300 K. According to Fig. 5(b), the decrease of thermal conductivity is dominated by a significant drop of τ_p of phonons with $\omega < 6$ THz, whereas the parameter V_g exhibits no obvious change (for more details, refer to the Supplemental Material). In addition, with the increase of tensile strain, the decrease of C_v and the increase of Grüneisen parameter γ, as shown in Fig. 5(b), proves that the in-plane tensile strain weakens the bonding strength and enhances the anharmonic. Weaker bonding strength can reduce the phonon frequency, resulting in a red shift of the phonon vibration mode in the phonon spectrum, which is proved in Fig. S7 within the Supplemental Material.

Therefore, strain engineering can simultaneously adjust the electronic structure and phonon transmission performance. In particular, the dual effects of the adjustment of the valence band and the suppression of phonon transmission are thus the reason for a noticeable increase in the value of ZT_{max} for *p*-type BiOCl. This could be concluded from the plots in Fig. 6. Under a certain strain, the

ZT_{max} values of *p*-type BiOCl [Fig. 6(c)] tend to increase linearly with increasing temperature. And the greater is the strain, the larger is the linear slope of ZT_{max} with temperature, meaning that the more significant is the strain-induced improvement in high-temperature thermoelectric performance. From Fig. 6(b), the changes of tensile strain have little effect on the *PF* of *p*-type BiOCl in the whole temperature range, but has a great effect on the electronic thermal conductivity, as shown in Fig. 6(a). Moreover, the lattice thermal conductivity of BiOCl is strongly reduced with the increase of stress, as shown in Fig. 5(a). Therefore, in the entire temperature range (300–800 K), with the effect of tensile strain, the decrease of total thermal conductivity is the main reason for the increase in *ZT* of *p*-type BiOCl.

IV. CONCULSION

In conclusion, the thermoelectric transport of BiOCl is studied by first-principles calculations using Boltzmann transport theory. According to the findings, the *ZT* of *p*-type BiOCl along the in plane and out plane reached 0.3

and 1.1, respectively, at 800 K. In addition, the in-plane biaxial tensile strain is found to increase phonon scattering and to reduce phonon relaxation time, resulting in a significant decrease in phonon thermal conductivity along the in plane and out plane. This, in turn, led to a noticeable increase of ZT in the temperature range of 300 to 800 K. Moreover, the in-plane biaxial tensile strain is shown to optimize the valence-band structure of BiOCl. As a result, the band gap is reduced and BiOCl became a direct band-gap semiconductor. Finally, the thermoelectric performance of p-type BiOCl is significantly improved, and the value of n_{opt} of p-type BiOCl could be decreased by an order of magnitude. Therefore, strain engineering is an efficient way to improve thermoelectric performance of BiOCl, making them have potential for high-temperature TE applications.

SUPPLEMENTAL MATERIAL

See the Supplemental Material for the computational details of electronic and phonon transport.

ACKNOWLEDGMENTS

The data that support the findings in this paper are available from the corresponding author upon reasonable request.

[1] Y. Pei, H. Wang, and G. J. Snyder, Band engineering of thermoelectric materials, Adv. Mater. **24,** 6125 (2012).

[2] Y.-J. Zeng, D. Wu, X.-H. Cao, W.-X. Zhou, L.-M. Tang, and K.-Q. Chen, Nanoscale organic thermoelectric materials: Measurement, theoretical models, and optimization strategies, Adv. Funct. Mater. **30,** 1903873 (2020).

[3] J. Park, Y. Xia, A. M. Ganose, A. Jain, and V. Ozoliņš, High Thermoelectric Performance and Defect Energetics of Multipocketed Full Heusler Compounds, Phys. Rev. Appl. **14,** 024064 (2020).

[4] C. Zhang, D. Ma, M. Shang, X. Wan, J.-T. Lü, Z. Guo, B. Li, and N. Yang, Graded thermal conductivity in 2D and 3D homogeneous hotspot systems, Mater. Today Phys. **22,** 100605 (2022).

[5] M. Baitinger, H. D. Nguyen, C. Candolfi, I. Antonyshyn, K. Meier-Kirchner, I. Veremchuk, V. Razinkov, M. Havryluk, R. Cardoso-Gil, and U. Burkhardt, Thermoelectric characterization of the clathrate-I solid solution $Ba_{8-\delta}Au_xGe_{46-x}$, Appl. Phys. Lett. **119,** 063902 (2021).

[6] D. Wu, X.-H. Cao, S.-Z. Chen, L.-M. Tang, Y.-X. Feng, K.-Q. Chen, and W.-X. Zhou, Pure spin current generated in thermally driven molecular magnetic junctions: A promising mechanism for thermoelectric conversion, J. Mater. Chem. A **7,** 19037 (2019).

[7] H. H. Huang, X. Fan, D. J. Singh, and W. T. Zheng, Thermoelectric properties of monolayer GeAsSe and SnSbTe, J. Mater. Chem. C **8,** 9763 (2020).

[8] B. Ryu, J. Chung, E.-A. Choi, P. Ziolkowski, E. Müller, and S. Park, Counterintuitive example on relation between ZT and thermoelectric efficiency, Appl. Phys. Lett. **116,** 193903 (2020).

[9] J. Mao, G. Chen, and Z. Ren, Thermoelectric cooling materials, Nat. Mater. **20,** 454 (2021).

[10] A. Kommini and Z. Aksamija, Anisotropic Thermoelectric Power Factor of Two-Dimensional Materials with Periodic Potential Barriers: The Wigner-Rode Formalism, Phys. Rev. Appl. **14,** 034037 (2020).

[11] M. Jonson and G. D. Mahan, Mott's formula for the thermopower and the Wiedemann-Franz law, Phys. Rev. B **21,** 4223 (1980).

[12] L. D. Hicks and M. S. Dresselhaus, Thermoelectric figure of merit of a one-dimensional conductor, Phys. Rev. B **47,** 16631 (1993).

[13] A. Suwardi, J. Cao, Y. Zhao, J. Wu, S. W. Chien, X. Y. Tan, L. Hu, X. Wang, W. Wang, D. Li, Y. Yin, W.-X. Zhou, D. V. M. Repaka, J. Chen, Y. Zheng, Q. Yan, G. Zhang, and J. Xu, Achieving high thermoelectric quality factor toward high figure of merit in GeTe, Mater. Today Phys. **14,** 100239 (2020).

[14] A. Suwardi *et al.*, Tailoring the phase transition temperature to achieve high-performance cubic GeTe-based thermoelectrics, J. Mater. Chem. A **8,** 18880 (2020).

[15] X.-K. Chen and K.-Q. Chen, Thermal transport of carbon nanomaterials, J. Phys-Condens. Matter **32,** 153002 (2020).

[16] Y. Gu, Mode-dependent phonon transmission in a T-shaped three-terminal graphene nanojunction, Carbon **158,** 818 (2020).

[17] S. Li, X. Liu, Y. Liu, F. Liu, J. Luo, and F. Pan, Optimized hetero-interfaces by tuning 2D SnS_2 thickness in $Bi_2Te_{2.7}Se_{0.3}/SnS_2$ nanocomposites to enhance thermoelectric performance, Nano Energy **39,** 297 (2017).

[18] S. Li, C. Xin, X. Liu, Y. Feng, Y. Liu, J. Zheng, F. Liu, Q. Huang, Y. Qiu, and J. He, 2D hetero-nanosheets to enable ultralow thermal conductivity by all scale phonon scattering for highly thermoelectric performance, Nano Energy **30,** 780 (2016).

[19] Z.-X. Xie, Y. Zhang, X. Yu, K.-M. Li, and Q. Chen, Ballistic thermal conductance by phonons through superlattice quantum-waveguides, J. Appl. Phys. **115,** 104309 (2014).

[20] Q. D. Gibson, T. Zhao, L. M. Daniels, H. C. Walker, R. Daou, S. Hébert, M. Zanella, M. S. Dyer, J. B. Claridge, and B. Slater, Low thermal conductivity in a modular inorganic material with bonding anisotropy and mismatch, Science **373,** 1017 (2021).

[21] W.-X. Zhou, D. Wu, G. Xie, K.-Q. Chen, and G. Zhang, α-Ag_2S: A ductile thermoelectric material with high ZT, ACS Omega **5,** 5796 (2020).

[22] Y. Wu, Z. Chen, P. Nan, F. Xiong, S. Lin, X. Zhang, Y. Chen, L. Chen, B. Ge, and Y. Pei, Lattice strain advances thermoelectrics, Joule **3,** 1276 (2019).

[23] C.-M. Lin, W.-C. Chen, and C.-C. Chen, First-principles study of strain effect on the thermoelectric properties of LaP and LaAs, Phys. Chem. Chem. Phys. **23,** 18189 (2021).

[24] S.-D. Guo, Biaxial strain tuned thermoelectric properties in monolayer PtSe$_2$, J. Mater. Chem. C **4**, 9366 (2016).

[25] Q. Wang, L. Han, L. Wu, T. Zhang, S. Li, and P. Lu, Strain effect on thermoelectric performance of InSe monolayer, Nanoscale Res. Lett. **14**, 1 (2019).

[26] S. Hu, J. Chen, N. Yang, and B. Li, Thermal transport in graphene with defect and doping: Phonon modes analysis, Carbon **116**, 139 (2017).

[27] J. Liu, T. Xing, Z. Gao, J. Liang, L. Peng, J. Xiao, P. Qiu, X. Shi, and L. Chen, Enhanced thermoelectric performance in ductile Ag$_2$S-based materials via doping iodine, Appl. Phys. Lett. **119**, 121905 (2021).

[28] W.-X. Zhou, Y. Cheng, K.-Q. Chen, G. Xie, T. Wang, and G. Zhang, Thermal conductivity of amorphous materials, Adv. Func. Mater. **30**, 1903829 (2020).

[29] B. C. Gu, Z. Li, J. D. Liu, H. J. Zhang, and B. J. Ye, Effect of vacancies on thermoelectric properties of β-CuAgSe studied by positron annihilation, Appl. Phys. Lett. **115**, 192106 (2019).

[30] D. Han, X. Yang, M. Du, G. Xin, J. Zhang, X. Wang, and L. Cheng, Improved thermoelectric properties of WS$_2$–WSe$_2$ phononic crystals: Insights from first-principles calculations, Nanoscale **13**, 7176 (2021).

[31] C.-W. Wu, C. Xiang, H. Yang, W.-X. Zhou, G. Xie, B. Ou, and D. Wu, Enhanced thermoelectric properties in two-dimensional monolayer Si2BN by adsorbing halogen atoms, Chin. Phys. B **30**, 037304 (2021).

[32] P.-Z. Jia, Y.-J. Zeng, D. Wu, H. Pan, X.-H. Cao, W.-X. Zhou, Z.-X. Xie, J.-X. Zhang, and K.-Q. Chen, Excellent thermoelectric performance induced by interface effect in MoS2/MoSe2 van der Waals heterostructure, J. Phys. Condens. Matter. **32**, 055302 (2019).

[33] V.-T. Tran, J. Saint-Martin, P. Dollfus, and S. Volz, High thermoelectric performance of graphite nanofibers, Nanoscale **10**, 3784 (2018).

[34] D. Parker, X. Chen, and D. J. Singh, High Three-Dimensional Thermoelectric Performance from Low-Dimensional Bands, Phys. Rev. Lett. **110**, 146601 (2013).

[35] D. Wu, X.-H. Cao, P.-Z. Jia, Y.-J. Zeng, Y.-X. Feng, L.-M. Tang, W.-X. Zhou, and K.-Q. Chen, Excellent thermoelectric performance in weak-coupling molecular junctions with electrode doping and electrochemical gating, Sci. China Phys. Mech. **63**, 276811 (2020).

[36] X.-K. Chen, X.-Y. Hu, P. Jia, Z.-X. Xie, and J. Liu, Tunable anisotropic thermal transport in porous carbon foams: The role of phonon coupling, Inte. J. Mech. Sci. **206**, 106576 (2021).

[37] D. Wu, L. Huang, P.-Z. Jia, X.-H. Cao, Z.-Q. Fan, W.-X. Zhou, and K.-Q. Chen, Tunable spin electronic and thermoelectric properties in twisted triangulene π-dimer junctions, Appl. Phys. Lett. **119**, 063503 (2021).

[38] M. N. Çınar and H. Sevinçli, Dimensional Crossover and Enhanced Thermoelectric Efficiency Due to Broken Symmetry in Graphene Antidot Lattices, Phys. Rev. Appl. **14**, 024075 (2020).

[39] L. Kang, X. Yu, X. Zhao, Q. Ouyang, J. Di, M. Xu, D. Tian, W. Gan, C. C. Ang, and S. Ning, Space-confined microwave synthesis of ternary-layered BiOCl crystals with high-performance ultraviolet photodetection, InfoMat **2**, 593 (2020).

[40] J. Li, H. Li, G. Zhan, and L. Zhang, Solar water splitting and nitrogen fixation with layered bismuth oxyhalides, Acc. Chem. Res. **50**, 112 (2017).

[41] H. Li, J. Li, Z. Ai, F. Jia, and L. Zhang, Oxygen vacancy-mediated photocatalysis of BiOCl: Reactivity, selectivity, and perspectives, Angew Chem. Int. Ed. Engl. **57**, 122 (2018).

[42] J. Jiang, K. Zhao, X. Xiao, and L. Zhang, Synthesis and facet-dependent photoreactivity of BiOCl single-crystalline nanosheets, J. Am. Chem. Soc. **134**, 4473 (2012).

[43] J. Lu, W. Zhou, X. Zhang, and G. Xiang, Electronic structures and lattice dynamics of layered BiOCl single crystals, J. Phys. Chem. Lett. **11**, 1038 (2020).

[44] G. Kresse and J. Furthmüller, Efficient iterative schemes for ab initio total-energy calculations using a plane-wave basis set, Phys. Rev. B **54**, 11169 (1996).

[45] J. P. Perdew, K. Burke, and M. Ernzerhof, Generalized Gradient Approximation Made Simple, Phys. Rev. Lett. **77**, 3865 (1996).

[46] W. Li, J. Carrete, N. A. Katcho, and N. Mingo, ShengBTE: A solver of the Boltzmann transport equation for phonons, Comput. Phys. Commun. **185**, 1747 (2014).

[47] A. Togo and I. Tanaka, First principles phonon calculations in materials science, Scripta Mater. **108**, 1 (2015).

[48] M. D. Santia, N. Tandon, and J. D. Albrecht, Lattice thermal conductivity in β-Ga$_2$O$_3$ from first principles, Appl. Phys. Lett. **107**, 041907 (2015).

[49] J. Yu and Q. Sun, Bi$_2$O$_2$Se nanosheet: An excellent high-temperature n-type thermoelectric material, Appl. Phys. Lett. **112**, 053901 (2018).

[50] J. Yu, T. Li, G. Nie, B.-P. Zhang, and Q. Sun, Ultralow lattice thermal conductivity induced high thermoelectric performance in the δ-Cu$_2$S monolayer, Nanoscale **11**, 10306 (2019).

[51] N. Wang, M. Li, H. Xiao, X. Zu, and L. Qiao, Layered La Cu O Se: A Promising Anisotropic Thermoelectric Material, Phys. Rev. Appl. **13**, 024038 (2020).

[52] H. Lang, S. Zhang, and Z. Liu, Mobility anisotropy of two-dimensional semiconductors, Phys. Rev. B **94**, 235306 (2016).

[53] T. Zhao, Q. D. Gibson, L. M. Daniels, B. Slater, and F. Cora, Prediction of higher thermoelectric performance in BiCuSeO by weakening electron–polar optical phonon scattering, J. Mater. Chem. A **8**, 25245 (2020).

[54] See Supplemental Material at http://link.aps.org/supplemental/10.1103/PhysRevApplied.18.014053 for band-edge energy as a function of strain.

[55] See Supplemental Material at http://link.aps.org/supplemental/10.1103/PhysRevApplied.18.014053 for the elastic modulus, DP constant, and effective mass.

[56] G. Casu, A. Bosin, and V. Fiorentini, Efficient thermoelectricity in Sr$_2$Nb$_2$O$_7$ with energy-dependent relaxation times, Phys. Rev. Mater. **4**, 075404 (2020).

[57] See Supplemental Material at http://link.aps.org/supplemental/10.1103/PhysRevApplied.18.014053 for the required parameters of impurity and polarized optical phonon scattering calculation.

[58] See Supplemental Material at http://link.aps.org/supplemental/10.1103/PhysRevApplied.18.014053 for the thermoelectric properties, as shown in Fig. S2 to Fig. S5.

[59] N. T. Hung, A. R. Nugraha, and R. Saito, Designing high-performance thermoelectrics in two-dimensional tetradymites, Nano Energy **58**, 743 (2019).

[60] T. Nian, Z. Wang, and B. Dong, Thermoelectric properties of α-In$_2$Se$_3$ monolayer, Appl. Phys. Lett. **118**, 033103 (2021).

[61] H. Peng, N. Kioussis, and D. A. Stewart, Anisotropic lattice thermal conductivity in chiral tellurium from first principles, Appl. Phys. Lett. **107**, 251904 (2015).

[62] G. J. Snyder and E. S. Toberer, Complex thermoelectric materials, Materials for sustainable energy: A collection of peer-reviewed research and review articles from Nature Publishing Group, 101 (2011).

[63] A. M. Ganose, S. Matsumoto, J. Buckeridge, and D. O. Scanlon, Defect Engineering of Earth-Abundant Solar Absorbers BiSI and BiSeI, Chem. Mater. **30**, 3827 (2018).

[64] See Supplemental Material at http://link.aps.org/supplemental/10.1103/PhysRevApplied.18.014053 for the band structure of BiOCl under different strain.

[65] T. Feng, A. O'hara, and S. T. Pantelides, Quantum prediction of ultra-low thermal conductivity in lithium intercalation materials, Nano Energy **75**, 104916 (2020).

[66] See Supplemental Material at http://link.aps.org/supplemental/10.1103/PhysRevApplied.18.014053 for the normalized accumulated thermal conductivity as a function of frequency.